ACS Photonics

Open Access

This article is licensed under CC-BY 4.0

pubs.acs.org/journal/apchd5

Article

High-Spatial-Resolution Near-Infrared Thermography Using an Uncooled Silicon-Based Camera

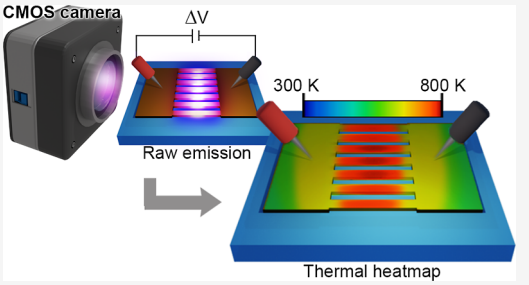
Ilario Bisignano, Po-Sheng Shih, Masataka Imura, Kuo-Ping Chen, and Satoshi Ishii*

Cite This: *ACS Photonics* 2026, 13, 5139−5146

Read Online

ACCESS | Metrics & More | Article Recommendations | Supporting Information

ABSTRACT: The demand for noncontact temperature measurements is growing as the microelectronic features to be probed become progressively smaller. However, traditional thermal imaging with infrared cameras is fundamentally constrained by the micron-long wavelength of thermal emission. In this study, we explore a cost-effective, high-spatial-resolution thermography technique utilizing an uncooled silicon CMOS camera with an optical microscope setup. By detecting the integrated near-infrared (NIR, 700−1100 nm) thermal emission from Joule-heated metallic microstructures, our method successfully bypasses the traditional microbolometer's diffraction limit and spatial resolution constraints. To ensure accurate temperature estimation, the camera is calibrated by leveraging the temperature-dependent Raman peak shift of hexagonal boron nitride flakes. Our optical microscope setup is in an oversampling condition, allowing us to exploit digital binning to achieve significant noise reduction and to directly visualize and map thermal emission at temperatures as low as 413 K for our titanium sample, which has an emissivity of around 0.4 in the NIR. This method provides a robust, highly capable tool for diagnosing localized thermal bottlenecks and mapping heat diffusion in high-density microelectronics.



KEYWORDS: *thermography, CMOS camera, thermal radiation, Joule heating, thermal mapping, microelectronics*

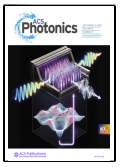
INTRODUCTION

The need for noncontact temperature measurements is increasing as the features to be probed become progressively smaller, rendering contact measurements challenging. Thermography is a noncontact temperature-mapping method widely used for various purposes. To achieve high resolutions approaching the diffraction limit, quantum-type photon detectors using materials such as InSb and HgCdTe are typically required. However, these costly sensors must be cooled to liquid nitrogen temperatures to suppress thermally generated dark currents. The need for constant cooling, combined with the finite lifespan of the cooling equipment, makes high-resolution thermal cameras prohibitively expensive and complex. This economic and technical disparity is the driving force behind our investigation into more approachable alternatives.

A bolometer-type camera is another type that is relatively inexpensive and compact. The core functional mechanism of a bolometer is its capability to absorb infrared radiation, leading to a change in electrical resistivity (resistance-type bolometer) or forward voltage (diode-type bolometer), allowing the formation of a thermal image through the interface circuitry.[1] The pixel size of microbolometers has decreased over the past few decades[2−13] (see Figure S1); however, further size reduction has stalled as the pixel size approaches the diffraction limit. In addition, a smaller pixel size results in lower sensitivity in general, nevertheless, it is worth mentioning the recent effort to enhance the absorption, for example, by integrating metasurfaces,[14] or umbrella absorbers[15] or to improve the photocurrent conversion within the read-out integrated circuit (ROIC).[16]

In contrast, using silicon (Si) as a cost-effective alternative relies on the photoelectric effect as the primary detection mechanism, effectively combining the advantages of both uncooled and cooled detectors. This method requires the incident photon to possess energy higher than the bandgap energy. For crystalline Si at room temperature, the bandgap energy is approximately 1.12 eV,[17] corresponding to a cutoff wavelength of approximately 1100 nm. According to Planck's law, the spectral radiance of an object at room temperature is concentrated in the mid- to far-infrared. However, as an object temperature increases, the high-energy tail of its thermal emission spectrum begins to overlap with the NIR responsivity of Si, yielding a photon flux capable of overcoming the noise floor of standard semiconductor sensors.[18] Accurate temperature measurements utilizing Si CMOS cameras have been previously demonstrated using two-color pyrometry.[19,20] This

Received: May 12, 2026
Revised: August 6, 2026
Accepted: August 6, 2026
Published: August 12, 2026



ACS Publications

© 2026 The Authors. Published by American Chemical Society

https://doi.org/10.1021/acsphotonics.6c01167
ACS Photonics 2026, 13, 5139−5146

Downloaded from pubs.acs.org/apchd5/article-pdf/13/17/5139/6652304/acsphotonics.6c01167.pdf by NATL INST FOR MATLS SCIENCE (NIMS) user on 26 October 2026

technique estimates the object temperature by comparing the intensity of the emitted radiation at two wavelengths (or color channels, hence the name) against the theoretical ratio calculated from Planck's law. While utilizing narrow bandpass filters improves accuracy by closely approximating the monochromatic assumption of this law,[21] it inherently reduces the collected photon flux. Consequently, higher object temperatures are required to maintain a detectable signal-to-noise ratio. Conversely, color CMOS and CCD cameras offer a highly practical alternative by exploiting their inherent RGB Bayer filter.[22] By utilizing color sensors, researchers can achieve high-resolution, single-shot temperature mapping while maintaining a cost-effective and convenient setup.[23]

In this paper, we demonstrate the potential of an uncooled Si CMOS camera for high-spatial-resolution thermography by detecting the accumulated intensity of the near-infrared thermal emission from metallic microstructures such as gold (Au), titanium (Ti), aluminum (Al), or copper (Cu). The purpose of imaging different metals is to confirm the versatility of the measurement method. Some of these materials exhibit very low emissivity in the long-wave infrared (Au, for example, has an emissivity of 0.03), making traditional microbolometer measurements susceptible to environmental reflections and poor signal-to-noise ratios. Our method enables high-contrast imaging of these metals and is not substrate dependent, which allowed us to image on transparent borosilicate glass substrates without requiring emissive coatings,[24] significantly expanding the applicability of our method. While the demonstrations were done only with a Si CMOS camera, a Si CCD camera with sufficient sensitivity can also be used. This capability is critical for diagnosing localized thermal bottlenecks, such as submicron hot spots and junction-point gradients. For instance, in AlGaN/GaN high electron mobility transistors, high operational heat flux frequently leads to the formation of submicron hotspots.[25] This heating can cause severe reliability issues, including thermal droop[26] and overall performance degradation.[27] We present a valid yet niche solution for investigating such systems that govern reliability and electromigration in high-density microelectronics.

METHODS

All the samples except the AlGaN/GaN sample were fabricated on borosilicate glass substrates. The Cu, Al and Au samples consisted of a 15 nm Ti adhesion layer followed by a 50 nm thick Cu layer or a 100 nm thick Al/Au layer, respectively. The Ti sample consisted of a single 100 nm layer of Ti. A comprehensive breakdown of all the sample configurations is provided in Table S1. The patterns for metal deposition were defined via a tabletop maskless lithography system (μPG 101, Heidelberg Instruments Mikrotechnik GmbH) after spin-coating (Opticoat MS-A100, MIKASA CO., LTD) a diluted positive photoresist (TLOR-P003HP in a 1:0.5 ratio with 2-heptanone) at 5000 rpm. The AlGaN/GaN sample was prepared via metal−organic chemical vapor deposition, as in our previous work,[28] and the Au array (250 nm in size, 5 μm periodicity, 50 nm thick) has been fabricated via electron beam lithography. Thermal emission from the test samples was induced via Joule heating by applying a DC bias with a source-measure unit (Keithley 2400, TEKTRONIX, INC.).

Thermal emission images were acquired using an uncooled Si CMOS camera (VEX830, Wraymer Inc.) with a back-illuminated CMOS image sensor (IMX485, SONY), in which the standard IR-cut filter was replaced with an antireflection filter exhibiting >90% transmittance at wavelengths longer than 700 nm. The camera was mounted on a customized optical microscope setup designed to direct the emission, collected by a 50× (MXPLFLN50X, Evident; 0.8 NA) objective lens, into a spectrometer (IsoPlane 81, Teledyne Technologies Inc.). This spectrometer was calibrated using a tungsten halogen lamp (Thorlabs SLS201L/M). To provide sufficient distance between the sample and the objective lens for the probes to contact the sample, a 5× objective (GLI-PLACH5XLM, Wraymer Inc., 0.12 NA) and a 50× long-working-distance objective (SLMPLN50X, Evident, 0.35 NA) were employed. The images used for the temperature maps were saved as RGB24 demosaiced BMP files and imported as grayscale images into software (Gwyddion) using the RGB-sum option. Therefore, the analyzed scalar intensity corresponds to the sum of the 8-bit RGB channel values, rather than raw sensor counts. The same acquisition, export, and Gwyddion import procedures were applied to the calibration images and the measured thermal images, so the temperature calibration was performed directly on this RGB-sum intensity scale. Exposure time (5 s) and camera gain (×5000) were kept fixed for all calibration and measurement images. Automatic image-processing functions, including gamma correction, white balance, and contrast enhancement, were disabled or forced to default to ensure consistency between images.

The temperature of the Joule-heated samples was estimated by observing the temperature-dependent Raman peak shift of an hBN flake transferred onto the emitting segment. Raman spectra were excited using a 532 nm laser (CNI MSL-FN-532, CNI) and collected by a VIS-NIR spectrometer (Acton SP2300, Princeton Instruments). Finally, the thermal maps generated from the CMOS camera images were compared with thermal images obtained using an uncooled IR camera (VarioCam xHD 675, InfraTec GmbH) equipped with a 0.5× (0.5 NA) objective lens. The camera has a pixel size of 24 μm and its spectral range is 7.5−14 μm.

RESULTS AND DISCUSSION

Figure 1 shows a thermal image of a test sample acquired using the uncooled microbolometer IR camera with a 0.5× objective lens. The test sample consisted of periodically aligned 30 μm wide and 250 μm long Au strips, which were connected to contact pads, and electrical contacts were obtained with two metallic probes. When taking an image, the distinction between sensor resolving power and optical resolution should be acknowledged. The optical resolution is limited by the diffraction of the probed wavelength. The sensor resolving power was calculated by dividing the length of a known object by the number of pixels that formed the object image. For the IR camera, the spatial resolution of the sensor was ∼23 μm. As shown in Figure 1a top, the 30 μm wide features of the Au strips under bias are unresolved, leading to inaccurate temperature readings. A room-temperature, unbiased image of the sample is presented alongside a biased one for comparison (Figure 1a, bottom). The apparent higher temperature of the metal was caused by reflections from the camera's blackbody emission at around 305 K, as shown in Figure S2. Only the larger 250 μm features provide partial information regarding the sample's thermal gradient and spatial morphology. In contrast, the significantly smaller pixel size of the CMOS camera (2.9 μm) provides detailed spatial imaging as shown in Figure 1b. In order to achieve high spatial resolution and maintain the diffraction-limited resolution of the objective, pixels per diffraction-spot radius, or resolution distance, calculated from eq 1 needs to be larger than 2.[29]

$$\text{Pixels-per-diffraction spot radius} = \frac{0.61\lambda}{\text{NA}} \times \frac{\text{magnification}}{\text{CCD pixel size}} \quad (1)$$

A pixel-per-diffraction-spot radius >2 ensures that the Nyquist limit is met, capturing spatial details of the sample and avoiding pixelation and aliasing. Our current setup, with

Downloaded from pubs.acs.org/apchd5/article-pdf/13/17/5139/6652304/acsphotonics.6c01167.pdf by NATL INST FOR MATLS SCIENCE (NIMS) user on 26 October 2026

https://doi.org/10.1021/acsphotonics.6c01167
ACS Photonics 2026, 13, 5139−5146

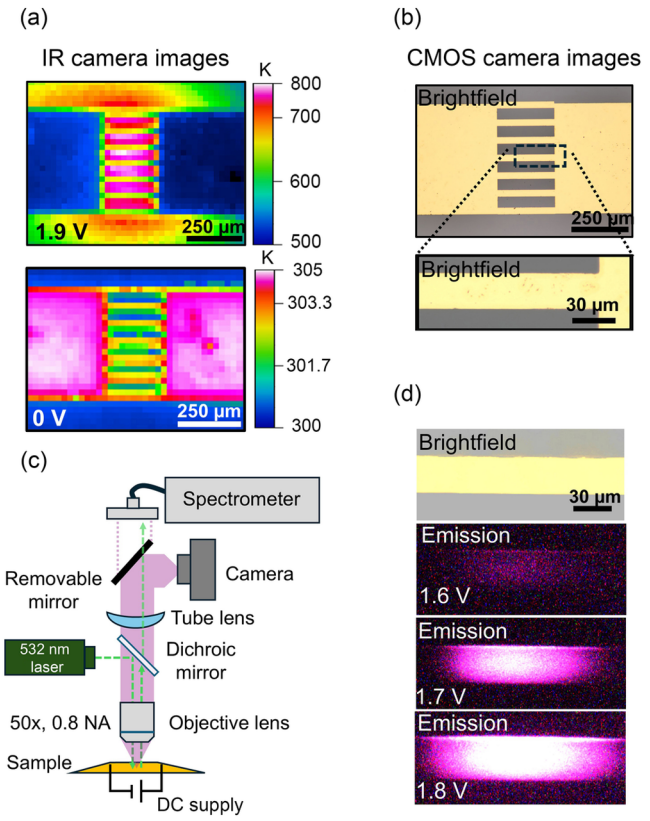


Figure 1. (a) IR camera image of the pattern Au sample that was Joule heated by applying a DC bias of 1.9 V (top) and no heating (bottom). The temperature reading on the Au area of the room temperature image is due to the reflection of the actual camera above it, emitting at 305 K (32 °C). The image was taken with a 0.5× objective lens. Visible bright-field optical microscope images (b) of the identical sample taken with a 5× objective lens and a 50× objective lens. (c) Schematic representation of the optical setup. (d) Brightfield and emission images of an Au strip showing higher emission intensities at higher applied DC bias (noted in the bottom left corner).

the 50× objective lens, 0.8 NA, and 2.9 μm pixel size, at a wavelength of 800 nm, provides a pixels-per-diffraction-spot radius of ∼10. This means there are 10 pixels per diffraction spot. This spatial oversampling validates the subsequent use of digital binning, which enhances the signal-to-noise ratio (SNR) without compromising the achievable optical resolution. A schematic representation of the optical setup is presented in Figure 1c.

When a DC voltage was applied to the two electrical contact pads, the central section of the metallic strips began emitting, which was captured by the CMOS camera. As the applied voltage increased, the camera recorded a clear monotonic increase in emission intensity (Figure 1d). The pixels appeared in a purple/magenta hue because the relative response of the CMOS camera's Bayer filter in the NIR region exhibited a slightly lower sensitivity in the green pixels at approximately 800 nm, as shown in Figure S3b. The internal signal processor (ISP) applies a higher gain to the red and blue channels to balance Si's natural higher sensitivity in the green wavelengths, accentuating this RGB response imbalance in the NIR region.

Before proceeding with further analysis and calibration, we ascertained the thermal origin of the observed emissions by directing emission from the metallic strip into a spectrometer equipped with a 100 μm-wide slit. The spectral response of the back-illuminated Si CCD detector was evaluated in advance by dividing the measured spectrum of a tungsten halogen lamp, which emits closely to an ideal blackbody at 2796 K, by the theoretical blackbody spectrum predicted by Planck's law multiplied by tungsten's emissivity. The emission spectra of the test samples were corrected by dividing the raw data by this response function. These corrected spectra were then fitted to Planck's law, with temperature as the fitting parameter. As shown in Figure S4, the data agree reasonably with the NIR blackbody tail of a graybody at 800−900 K, providing strong evidence for the thermal origin of the emission. The graybody fitting of the collected emission signal was mainly used to verify the thermal origin of the observed emission, whereas quantitative temperature calibration and camera-signal calibration were based on hBN Raman peak shifts as discussed in the following section.

Camera Calibration

Because the CCD of the spectrometer exhibited low responsivity beyond 900 nm, leading to unsatisfactory noise levels in the measured data, the CMOS camera was calibrated using Raman spectroscopy. By leveraging the temperature-dependent peak shift of hexagonal boron nitride (hBN), this approach yielded more accurate temperature estimations than the blackbody tail fitting. Among the three main hBN peaks, the doubly degenerate in-plane mode of the E_{2g} symmetry is the most sensitive to temperature.[30] In the current work, an hBN flake was transferred onto one of the Au strips. The sample was heated to various temperatures using a ceramic heater, and the resulting peak shifts were recorded, as shown in Figure S5. Determining the exact thickness of the flake is unnecessary in the high-temperature limit, as the E_{2g} peak shifts for single-layer, few-layer, and bulk hBN all exhibit a similar slope at temperatures above 300 K.[30] The calibration of emission intensity against applied voltage was performed on the portion of the flake located at the center of the Au strip, where emission is most pronounced, shown in Figure 2a.

Our custom optical setup allows for rapid switching between focusing the emission onto the CMOS camera (to record pixel intensity) and directing it to the spectrometer. The images at various applied voltages are shown in Figure 2b. The recorded peak centers and calculated temperatures from the Raman spectra are summarized in Figure 2c. The collected intensity from the sample was directly related to the sample temperature. More specifically, because the thermal spectrum for the investigated temperatures only lies in the lower sensitivity wavelength range of the camera due to Si's bandgap, limiting the integration wavelength range up to 1100 nm causes the camera signal to have a temperature dependence that can be steeper than the full spectrum Stefan−Boltzmann ($\propto T^4$) law. To account for this, the captured intensity was fitted with a general power law

$$M = a + bT^N \tag{2}$$

where, a is a small offset to account for stray light, which, together with b and N, become fitting parameters. The parameter T represents the temperature calculated from the hBN Raman shift, and the fitting points correspond to the averaged pixel intensities taken from an area on the Au strip adjacent to the hBN flake. The parameter b, by resemblance of Stefan−Boltzmann's radiant exitance ($R_E = \varepsilon\sigma T^4$), implicitly contains the material's emissivity ε. This fitted relation should,

Downloaded from pubs.acs.org/apchd5/article-pdf/13/17/5139/6652304/acsphotonics.6c01167.pdf by NATL INST FOR MATLS SCIENCE (NIMS) user on 26 October 2026

https://doi.org/10.1021/acsphotonics.6c01167
ACS Photonics 2026, 13, 5139−5146

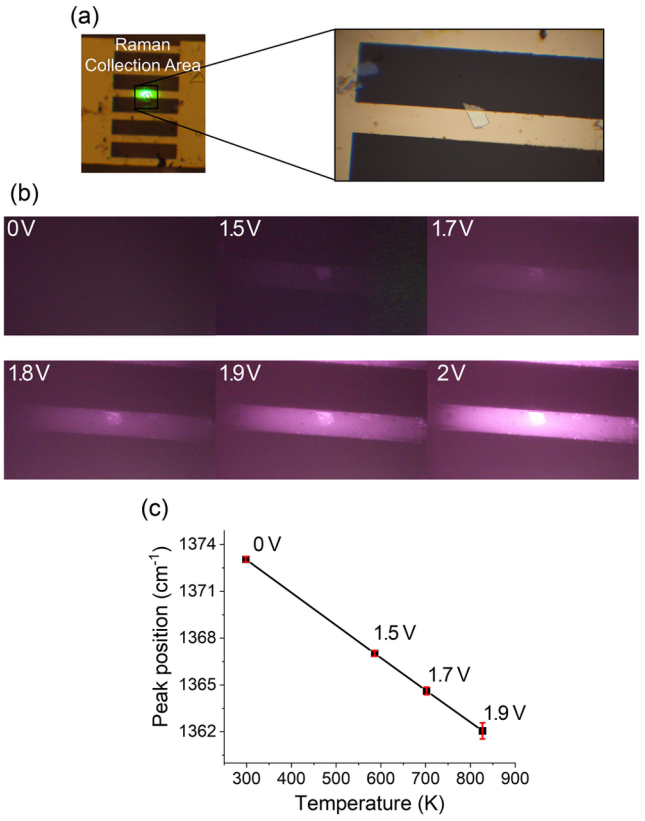


Figure 2. (a) Brightfield image of the sample used for calibration. The Raman collection area is highlighted by the green laser spot (left), a magnified image shows the hBN flake position on the Au strip (right). (b) Raw images of the calibration sample at different voltages (0 V−2 V, exposure time 5 s, gain × 5000). (c) Central peak wavenumbers of the Gaussian-fitted Raman spectra against the calculated temperature extrapolated from the temperature slope of the E_{2g} phonon mode of the hBN flake, measured at various DC Bias voltages, with error bars in red.

however, not be interpreted as a fundamental blackbody law, but as a semiempirical calibration function for the band-limited CMOS response, similar to the Sakuma−Hattori equations.[31] The fitting values together with their uncertainties are shown in Figure S6. The strong correlation between the fitted parameters b and N causes a relatively large uncertainty in these parameters. In the model used, changes in the exponent N can be partially compensated by changes in the proportionality factor b. To evaluate the uncertainty associated with the calibration model, the temperature residuals were calculated by comparing the temperatures predicted from the fitted power-law relation with the reference temperatures obtained from Raman thermometry. The standard deviation of these residuals was approximately 50 K. Assuming a direct relationship between the image intensity in grayscale and the fitted radiant exitance, the thermal mapping was performed by applying the inverse of eq 2 to calculate the temperature using 2D data processing and analysis software. In addition to globally subtracting the offset parameter a, an additional constant offset to correct for dark current effects was subtracted from each emission image by averaging the pixel intensity in an arbitrary area far from the emitting metallic strip, ensuring that only the background offset is computed. Each pixel intensity in the newly obtained image was then converted to temperature using an inverse formula via a user-defined function applied to each pixel. The resulting thermal maps are displayed in Figure 3. The CMOS camera captured a thermal gradient that increases toward the center of the Au strip. At higher voltages, it can spatially resolve the temperature gradient at the junction between the Au strip and the electrical contact pad on the top right corner. As the metallic strip was located at the upper edge of the contact pad, it experienced a reduction in width, causing a local change in the material's resistivity. Because of this local resistivity change, the Joule heating occurring in that area was slightly different from the surrounding metal, which was captured by our camera with a localized bright emission spot at the restricted area. The results offer a clear image of its potential use in electronic and microelectronic heat diffusion studies and analysis. Our experimental configuration enabled the direct visualization of thermal emission at temperatures as low as 600 K. This is represented in a highly detailed thermal map and indicates a lower detectable thermal threshold than previously reported values in the literature, which typically cite a lower limit of approximately 700 K for similar CMOS-based imaging techniques.[32,33]

While the proposed method has limitations, such as unwanted reflections, a minimum detectable temperature threshold, and noise management, the CMOS camera thermal mapping offers significant potential within its niche. It paves the way for a deeper understanding of temperature mapping in

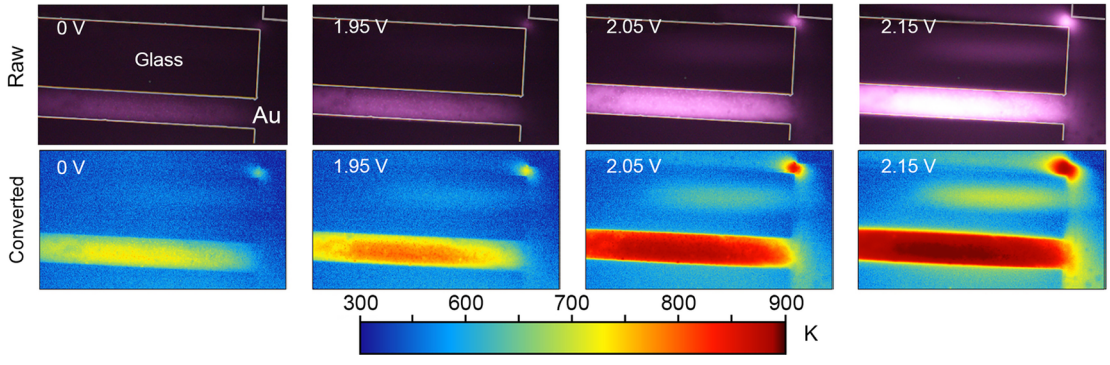


Figure 3. Top: raw images taken by the CMOS camera at the specified DC bias applied to the Au strip without digital binning; the strip edges are superimposed for clearer visualization. In this configuration, the electrical contact pads are positioned on the left and right boundaries of the strip. The localized hotspot discussed in the main text corresponds to the highly emitting region observed in the upper-right quadrant of the images. Bottom: thermal mapping of the corresponding raw images after the calibration process.

https://doi.org/10.1021/acsphotonics.6c01167
ACS Photonics 2026, 13, 5139−5146

Downloaded from pubs.acs.org/apchd5/article-pdf/13/17/5139/6652304/acsphotonics.6c01167.pdf by NATL INST FOR MATLS SCIENCE (NIMS) user on 26 October 2026

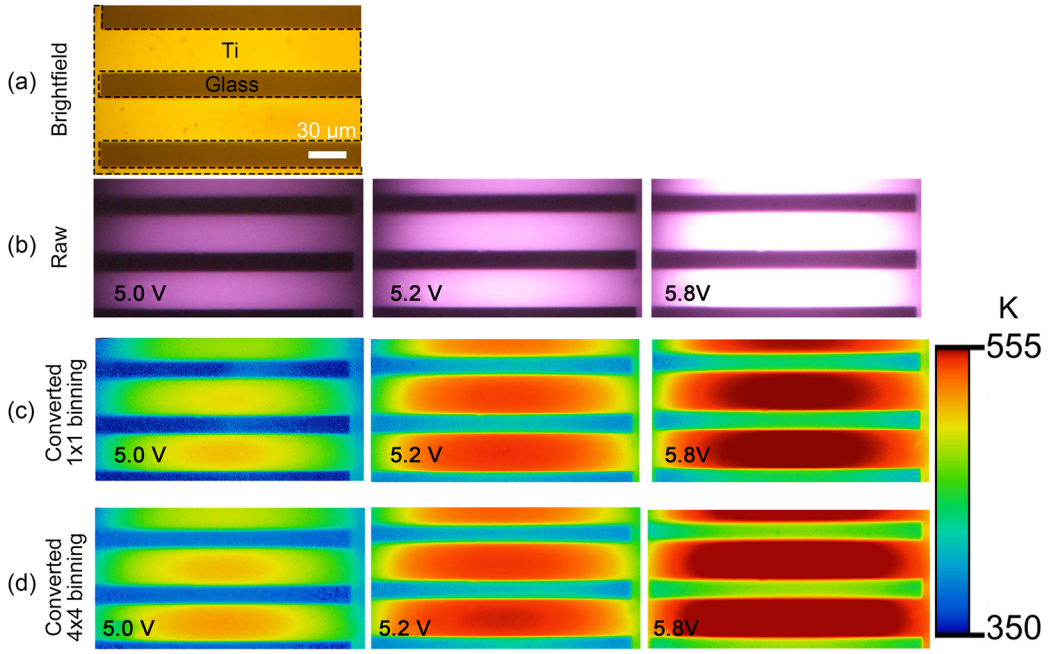


Figure 4. (a) Brightfield image of the Ti strips on a glass substrate. (b) Raw images of the strip's emission at different voltages. Converted images to the thermal mapping at various applied voltages (c) without binning (i.e., 1 × 1 digital binning) and (d) 4 × 4 digital binning.

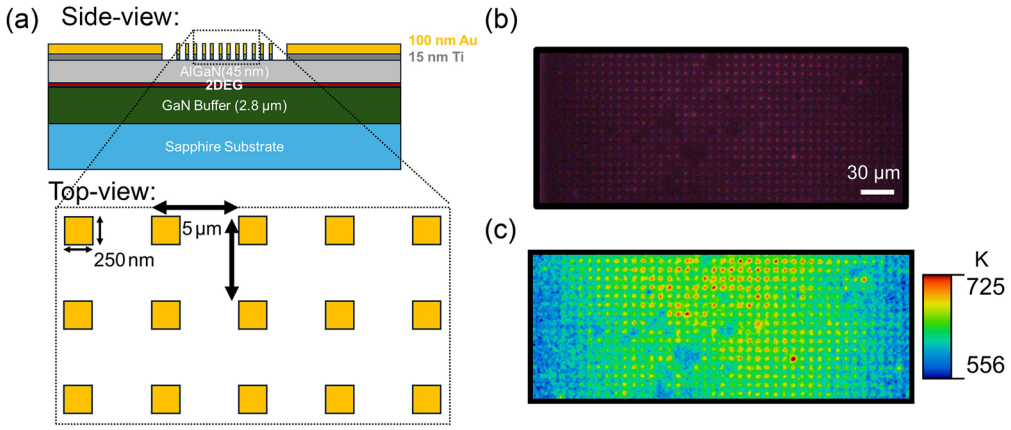


Figure 5. (a) Cross-section schematic (top) and top-view schematic (bottom) of the sample. (b) Raw NIR emission image of the sample. Heating was induced by applying a square wave voltage of 30 V at 34.5 kHz frequency with a 49% duty cycle to avoid damage. (c) Calibrated thermal map corresponding to the raw emission in (b), with a 4 × 4 digital binning applied.

submicron scale. To address these limitations, the detection of low-intensity radiation for emitter temperatures below approximately 700 K can be improved by fully exploiting the camera's high pixel resolution. Based on eq 1, the pixel-per-diffraction-spot-radius of around 10 allows us to use a binning of up to 55 while still barely staying below the Nyquist limit (2 pixels per diffraction-spot-radius). Because of this, a practical solution to increase sensitivity is to apply a 4 × 4 digital binning (to ensure it is well below the Nyquist limit), allowing the system to integrate the intensity over 16 pixels.

As proof of concept, images of the Ti sample emission were taken with both a 1 × 1 and a 4 × 4 binning. The raw images and their corresponding thermal maps are shown in Figure 4. These images exhibit very low background noise, and the reason for this is 2-fold. First, the 4 × 4 digital binning was set to average mode, averaging the signal over 16 pixels, effectively reducing the noise by a factor of 4. Second, the higher emissivity of Ti (approximately 0.4 in the NIR) yields much brighter thermal emission than Au (a 13-fold increase), giving a stark contrast between the emitting element and the background.

To understand the effect of the average digital binning, a quantitative SNR analysis was performed. By calculating the SNR as the ratio of the mean values to the standard deviation as $\mathrm{SNR} = \frac{\mu_{em} - \mu_{bg}}{\sigma_{bg}}$, where μ_{em} is the mean value of the pixel intensity at the center of the emitting strip averaged over a line containing more than 200 pixels; μ_{bg} the mean value of the dark/non emitting area of the image and σ_{bg} the standard deviation of the non emitting area. This analysis was performed on the Ti sample with a 5.5 V DC bias, where, under the same conditions, one image was taken with 1 × 1 average digital binning and one with 4 × 4 average digital binning. The results show a 2.2-fold (6.9 dB) increase in SNR when adopting a higher binning. Overall, the higher emissivity and the better

https://doi.org/10.1021/acsphotonics.6c01167
ACS Photonics 2026, 13, 5139−5146

Downloaded from pubs.acs.org/apchd5/article-pdf/13/17/5139/6652304/acsphotonics.6c01167.pdf by NATL INST FOR MATLS SCIENCE (NIMS) user on 26 October 2026

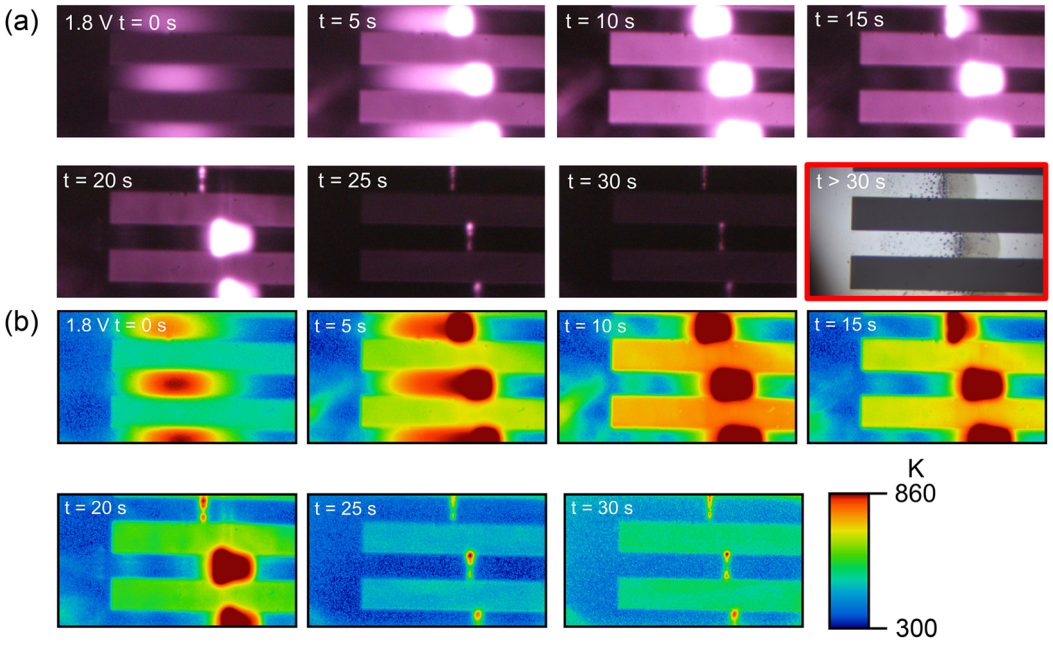


Figure 6. Time-resolved emission imaging of a 100 nm thick Al sample. Sequential frames (5 s exposure time) recorded at a constant 1.8 V DC bias depict the (a) raw emission intensity and (b) corresponding false-color thermal maps. The series illustrates the spatial migration of thermal hotspots along the metallic bridges, indicating dynamic structural reconfiguration. The image labeled as "t > 30 s" is the only bright-field image in the set, highlighted with a colored border.

SNR due to digital binning enabled the successful detection and thermal mapping of temperatures as low as 413 K.

To evaluate the ultimate resolving power of our methodology, we imaged 250 nm Au squares spaced periodically by 5 μm in the lateral direction on an AlGaN/GaN heterostructure. This specific architecture was chosen to mimic the highly localized, submicron thermal bottlenecks frequently observed in modern high-electron-mobility transistors. With a 50× objective lens, the emission from individual 250 nm Au squares was clearly distinguishable, as shown in Figure 5, successfully displaying a thermal map of distinct and periodic thermal emitters. The sharp contrast between the heated metallic squares and the underlying substrate confirms our system's capability to capture highly localized heat signatures. A more quantitative resolution metric was performed to obtain an experimental estimate of the effective spatial response. The measured edge-spread function (ESF), calculated line-spread function (LSF) and modulation transfer function (MTF) are displayed in Figure S7a–d. While AFM image comparison (Figure S7e) led to an edge response estimation of 1.7 μm, Figure 5c demonstrates that the system distinctly differentiates between adjacent emitters even with a 4 × 4 digital binning configuration active. This confirms that the operational spatial detection of the system outperforms the limitations implied by the ESF alone. Successfully resolving these micron features provides compelling experimental evidence that this uncooled CMOS technique is a highly viable tool for diagnosing micrometer-scale heat diffusion in next-generation microelectronics.

Additionally, Figure 6a presents the temporal evolution of both the raw optical emission and the processed thermal maps (Figure 6b) of an Al sample under a 1.8 V DC bias. After 5 s, the thermal map reveals a nonuniform temperature distribution along the metallic strip, with temperatures reaching around 900 K, close to the melting point of aluminum. This localization of heat suggests the presence of a structural bottleneck or resistive inhomogeneity. As the electrical strain continues, these hotspots migrate laterally. The progressive degradation eventually leads to a catastrophic loss of structural integrity. After 25 s, the strip yields, interrupting the electrical connection and causing the emission to vanish as the system returns to thermal equilibrium. The final bright-field frame (at t > 30 s) confirms significant morphological damage to the metallic strips. In the present demonstration, the 5 s exposure time was kept fixed to maintain consistency with the other measurements. It is, however, useful to discuss the temporal resolution limit of the system. This resolution limit depends heavily on factors such as temperature, emissivity, binning, and exposure time. Because the systematic measurement of dependence on all these factors falls outside the scope of our work, we do not currently assign a validated minimum exposure time. However, it is feasible to theoretically determine the minimum integration time limit achievable by the system. Based on the SNR analysis, reducing the exposure time to 1 s still yields a theoretically detectable signal. Furthermore, by exploiting a 4 × 4 sum binning instead of average binning, the minimum exposure time can be further reduced to ∼60 ms.

Finally, Figure S8 presents the thermal mapping and emission images of the Cu sample. Capturing bare Cu emission presented a unique challenge: we observed a change in optical appearance and a sudden change in applied current. It was assumed to be the Cu-oxidation at temperatures below the threshold required to observe NIR emission. Assuming the oxidation, its emissivity could be higher than that of Cu, resulting in brighter emission. Consequently, the aforementioned temperature mapping cannot be applied to this case, as the emissivity varies continuously along the metallic strip in tandem. The extracted thermal map should thus be considered qualitative, rather than quantitative, as the emissivity remains unknown and might have changed dynamically under the bias voltage. Herein lies an advantage of Si CMOS cameras over

Downloaded from pubs.acs.org/apchd5/article-pdf/13/17/5139/6652304/acsphotonics.6c01167.pdf by NATL INST FOR MATLS SCIENCE (NIMS) user on 26 October 2026

https://doi.org/10.1021/acsphotonics.6c01167
ACS Photonics 2026, 13, 5139−5146

conventional NIR-only cameras, such as InGaAs cameras. Because the Si CMOS sensor retains broad sensitivity across the visible spectrum, it potentially offers the ability to use the visible color to estimate the thickness of newly formed layer. A standard InGaAs camera, being grayscale and blind to these visible wavelengths, may miss capturing these vital visual changes. This dual capability underscores the distinct versatility of standard Si CMOS cameras for complex thermal diagnostics.

CONCLUSION

In this study, we demonstrated a cost-effective and comprehensive approach to high-spatial-resolution thermography using an uncooled Si CMOS camera. By detecting integrated NIR emission within the 700 to 1100 nm range, this method successfully bypasses the diffraction limit and high manufacturing costs that constrain traditional microbolometer-based thermal imaging. To ensure accurate temperature estimation, we calibrated the camera utilizing the temperature-dependent Raman peak shift of hBN flakes. This calibration enabled precise thermal mapping of Joule-heated Au microstrips and the detection of well-spaced submicron features with the electrical contact pads. While this technique is inherently constrained by sample emissivity, calibration assumptions, background subtraction, and image-processing conditions, a significant enhancement in sensitivity was achieved by exploiting the camera's digital binning function. Ultimately, this thermal mapping with a Si CMOS camera, and potentially with a Si CCD camera, offers a highly capable, specialized tool for advancing the analysis of heat diffusion and reliability in modern microelectronics.

ASSOCIATED CONTENT

Supporting Information

The Supporting Information is available free of charge at https://pubs.acs.org/doi/10.1021/acsphotonics.6c01167.

Evolution of reported microbolometer detector pixel pitch over time. (Supporting Information, Figure S1); sample configurations used in the present study (Supporting Information, Table S1); thermal image taken by an IR camera (Supporting Information, Figure S2); Sony StarVIS RBG relative response (Supporting Information, Figure S3); emission spectra of the 500 μm wide Au strips at different applied voltages (Supporting Information, Figure S4); details of the hBN temperature-to-peak shift calibration process (Supporting Information, Figure S5); measured cumulative pixel intensity and fitted power law model against temperature (Supporting Information, S6); fitted power law parameters with their respective standard deviations (Supporting Information, Table S2); quantitative resolution metrics for the CMOS camera (Supporting Information, S7); thermal mapping and emission images of the Cu sample (Supporting Information, Figure S8) (PDF)

AUTHOR INFORMATION

Corresponding Author

Satoshi Ishii − *Research Center for Materials Nanoarchitectonics (MANA), National Institute for Materials Science (NIMS), Ibaraki 305-0044, Japan; Graduate School of Science and Technology, University of Tsukuba, Ibaraki 305-8577, Japan;* orcid.org/0000-0003-0731-8428; Email: sishii@nims.go.jp

Authors

Ilario Bisignano − *Research Center for Materials Nanoarchitectonics (MANA), National Institute for Materials Science (NIMS), Ibaraki 305-0044, Japan; Graduate School of Science and Technology, University of Tsukuba, Ibaraki 305-8577, Japan;* orcid.org/0009-0004-9964-2106

Po-Sheng Shih − *Institute of Photonics Technologies, National Tsing Hua University, Hsinchu 300, Taiwan*

Masataka Imura − *Research Center for Electronic and Optical Materials, National Institute for Materials Science (NIMS), Ibaraki 305-0047, Japan;* orcid.org/0000-0002-4236-9549

Kuo-Ping Chen − *Institute of Photonics Technologies, National Tsing Hua University, Hsinchu 300, Taiwan*

Complete contact information is available at: https://pubs.acs.org/10.1021/acsphotonics.6c01167

Funding

S.I. acknowledges the support from JST FOREST (JPMJFR2139), Innovative Science and Technology Initiative for Security, Acquisition, Technology & Logistics Agency (ATLA, JPJ013268), and JSPS Kakenhi (22H01917, 24K21723, 26K22705). Part of this work was supported by the ARIM of MEXT (JPMXP1225NM5171, JPMXP1225NM5172, JPMXP1226NM5146, and JPMXP1226NM5147).

Notes

The authors declare no competing financial interest.

REFERENCES

(1) Fusetto, S.; Aprile, A.; Malcovati, P.; Bonizzoni, E. Readout IC Architectures and Strategies for Uncooled Micro-Bolometers Infrared Focal Plane Arrays: A Review. *Sensors* **2023**, *23*, 2727.

(2) Ishikawa, T.; Ueno, M.; Endo, K.; Nakaki, Y.; Hata, H.; Sone, T. Low-Cost 320 × 240 Uncooled IRFPA Using Conventional Silicon IC Process. *Proc. SPIE* **1999**, *3689*, 556−563.

(3) Ishikawa, T.; Ueno, M.; Nakaki, Y.; Endo, K.; Ohta, Y.; Nakanishi, J.; Kosasayama, Y.; Yagi, H.; Sone, T.; Kimata, M. Performance of 320 × 240 Uncooled IRFPA with SOI Diode Detectors. In *Infrared Technology and Applications XXVI*; Andresen, B. F., Fulop, G. F., Strojnik, M., Eds.; SPIE, 2000; Vol. *4130*, pp 152−159.

(4) Ueno, M.; Kosasayama, Y.; Sugino, T.; Nakaki, Y.; Fujii, Y.; Inoue, H.; Kama, K.; Seto, T.; Takeda, M.; Kimata, M. 640 × 480 Pixel Uncooled Infrared FPA with SOI Diode Detectors. In *Infrared Technology and Applications XXXI*; Andresen, B. F., Fulop, G. F., Eds.; SPIE, 2005; Vol. *5783*, pp 566−577.

(5) Seto, T.; Kama, K.; Kimata, M.; Takeda, M.; Hata, H.; Nakaki, Y.; Inoue, H.; Kosasayama, Y.; Ohta, Y.; Fukumoto, H. *60 × 120 Uncooled IRFPA for Small JR Camera*; R Discovery, 2006; pp 30−33.

(6) Fujisawa, D.; Maegawa, T.; Ohta, Y.; Kosasayama, Y.; Ohnakado, T.; Hata, H.; Ueno, M.; Ohji, H.; Sato, R.; Katayama, H.; Imai, T.; Ueno, M. Two-Million-Pixel SOI Diode Uncooled IRFPA with 15μm Pixel Pitch. In *Infrared Technology and Applications XXXVIII*; Andresen, B. F., Fulop, G. F., Norton, P. R., Eds.; SPIE, 2012; Vol. *8353*, pp 83531G−13.

(7) Muckensturm, K.-M.; Weiler, D.; Hochschulz, F.; Busch, C.; Geruschke, T.; Wall, S.; Heß, J.; Würfel, D.; Lerch, R.; Vogt, H. Measurement Results of a 12 Mm Pixel Size Microbolometer Array Based on a Novel Thermally Isolating Structure Integrated on a 17

Downloaded from pubs.acs.org/apchd5/article-pdf/13/17/5139/6652304/acsphotonics.6c01167.pdf by NATL INST FOR MATLS SCIENCE (NIMS) user on 26 October 2026

Mm ROIC. In *Infrared Technology and Applications XLII*; Andresen, B. F., Fulop, G. F., Hanson, C. M., Norton, P. R., Eds.; SPIE, 2016; Vol. *9819*, p 98191N.
(8) Liu, D.; Lu, W.; Chen, Z.; Zhang, Y.; Lei, S.; Tan, G. A 14-Bit Differential-Ramp Single-Slope Column-Level ADC for 640 × 512 Uncooled Infrared Imager. In *2016 IEEE International Symposium on Circuits and Systems (ISCAS)*, 2016; pp 1922−1925.
(9) Celik, O.; Inceturkmen, E.; Kaplan, B.; Barutcu, B.; Aydin, O.; Gonenli, I. E.; Kepenek, R.; Tunca, C.; Akbulut, M.; Nuzumlali, O.; Keskin, S.; Aydemir, K.; Yildizak, C. 640 × 480 17 Um Microbolometer Uncooled Detector Development at ASELSAN. In *Infrared Technology and Applications XLVI*; Andresen, B. F., Fulop, G. F., Miller, J. L., Zheng, L., Eds; SPIE, 2020; Vol. *11407*, p 1140719.
(10) Qiu, J.; Su, L.; McDowell, L. L.; Phan, Q.; Liu, Y.; Zhang, G.; Yang, Y.; Shi, Z. High-Performance Uncooled Mid-Infrared Detector Based on a Polycrystalline PbSe/CdSe Heterojunction. *ACS Appl. Mater. Interfaces* **2023**, *15* (20), 24541−24548.
(11) Chung, H.; Kwon, M.; Kang, S.-G. High-Resolution Uncooled Infrared Sensors: Innovations In 3d Mems Technology For Military Use. *2025 IEEE 38th International Conference on Micro Electro Mechanical Systems (MEMS)*, 2025; pp 189−192.
(12) Tanaka, A.; Matsumoto, S.; Tsukamoto, N.; Itoh, S.; Chiba, K.; Endoh, T.; Nakazato, A.; Okuyama, K.; Kumazawa, Y.; Hijikawa, M.; Gotoh, H.; Tanaka, T.; Teranishi, N. Infrared Focal Plane Array Incorporating Silicon IC Process Compatible Bolometer. *IEEE* **1996**, *43*, 1844−1850.
(13) Takamuro, D.; Maegawa, T.; Sugino, T.; Kosasayama, Y.; Ohnakado, T.; Hata, H.; Ueno, M.; Fukumoto, H.; Ishida, K.; Katayama, H.; Imai, T.; Ueno, M. Development of New SOI Diode Structure for beyond 17 Mm Pixel Pitch SOI Diode Uncooled IRFPAs. In *Infrared Technology and Applications XXXVII*; SPIE, 2011; Vol. *8012*, p 80121E.
(14) Zhang, X.; Liu, H.; Zhang, Z. G.; Wang, Q.; Zhu, S. N. Controlling Thermal Emission of Phonon by Magnetic Metasurfaces. *Sci. Rep.* **2017**, *7*, 41858.
(15) Erturk, O.; Akin, T. Design and Implementation of High Fill-Factor Structures for Low-Cost CMOS Microbolometers. In *2018 IEEE Micro Electro Mechanical Systems (MEMS)*, 2018; pp 692−695.
(16) Bhan, R. K.; Dhar, V. Recent Infrared Detector Technologies, Applications, Trends and Development of HgCdTe Based Cooled Infrared Focal Plane Arrays and Their Characterization. *Opto-Electron. Rev.* **2019**, *27* (2), 174−193.
(17) Sze, S. M.; Ng, K. K. *Physics of Semiconductor Devices*; Wiley-Interscience: New York, 1969.
(18) Saito, T.; Sakai, S.; Iizawa, I.; Suda, E.; Umetani, K.; Kaneko, K.; Furukawa, Y.; Ohkura, T. A New Technique of Radiation Thermometry Using a Consumer Digital Camcorder: Observations of Red Glow at Aso Volcano, Japan. *Earth Planet* **2005**, *57*, e5−e8.
(19) Jiménez, S. Two-Color, Two-Dimensional Pyrometers Based on Monochrome and Color Cameras for High-Temperature (> 1000 K) Planar Measurements. *Rev. Sci. Instrum.* **2020**, *91* (11), 114901.
(20) Chen, J.; Guo, Y.; Wang, D.; Xue, S.; Jiao, M.; Gao, C. A Data Processing Method for Two-Color Pyrometers in Accurate Temperature Measurement of High-Temperature Flow Fields. *Measurement* **2025**, *243*, 116431.
(21) Araujo, A. Multi-Spectral Pyrometry - A Review. In *Measurement Science and Technology*; Institute of Physics Publishing July, 2017; Vol. *17*.
(22) Deep, S.; Krishna, Y.; Jagadeesh, G. Temperature Characterization of a Radiating Gas Layer Using Digital-Single-Lens-Reflex-Camera-Based Two-Color Ratio Pyrometry. *Appl. Opt.* **2017**, *56* (30), 8492.
(23) Meriaudeau, F. Real Time Multispectral High Temperature Measurement: Application to Control in the Industry. *Image Vis. Comput.* **2007**, *25* (7), 1124−1133.
(24) Honnerová, P.; Veselý, Z.; Matějíček, J.; Honner, M. Coating Evaluation Methodology for Low-Temperature Thermographic Application. *Sci. Rep.* **2026**, *16* (1), 6090.
(25) Karim, A.; Shoemaker, D. C.; Kim, T. K.; Kwak, J. S.; Choi, S. Characterization of Hotspot Formation in AlGaN/GaN HEMTs by Probing Raman Scattering through an Optically Transparent Gate. *J. Appl. Phys.* **2025**, *138* (3), 034507.
(26) McAlister, S. P.; Bardwell, J. A.; Haffouz, S.; Tang, H. Self-Heating and the Temperature Dependence of the Dc Characteristics of GaN Heterostructure Field Effect Transistors. *J. Vac. Sci. Technol., A* **2006**, *24* (3), 624−628.
(27) Benbakhti, B.; Soltani, A.; Kalna, K.; Rousseau, M.; De Jaeger, J. C. Effects of Self-Heating on Performance Degradation in AlGaN/GaN-Based Devices. *IEEE Trans. Electron Devices* **2009**, *56* (10), 2178−2185.
(28) Bisignano, I.; Imura, M.; Tanjaya, N. K.; Ye, M. J.; Okada, N.; Ishii, S. Infrared Near-Field Spectroscopy of AlGaN/GaN Heterostructures for Probing Two-Dimensional Electron Gas. *ACS Appl. Mater. Interfaces* **2025**, *17* (35), 50077−50084.
(29) Murphy, D. B.; Davidson, M. W. Digital Image Processing. In *Fundamentals of Light Microscopy and Electronic Imaging*; John Wiley & Sons, Ltd, 2012; pp 415−449.
(30) Seremetis, L.; Koukaras, E. N.; Alexandri, S.; Michail, A.; Kalosakas, G.; Parthenios, J.; Galiotis, C.; Tsirkas, S.; Grammatikopoulos, S.; Papagelis, K.; Tsirkas, S.; Grammatikopoulos, S.; Grammatikopoulos, S.; Papagelis, K.; Papagelis, K. Thermomechanical Response of Supported Hexagonal Boron Nitride Sheets of Various Thicknesses. *J. Phys. Chem. C* **2020**, *124* (22), 12134−12143.
(31) Sakuma, F. Interpolation Equation of Scales of Radiation Thermometers. In *Proceedings of 6th International Symposium on Temperature and Thermal Measurements in Industry and Science in Torino*, 1996.
(32) Jackson, A. W.; Gossard, A. C. Thermal Imaging of Wafer Temperature in MBE Using a Digital Camera. *J. Cryst. Growth* **2007**, *301−302*, 105−108.
(33) Paquette, B.; Gsib, B.; Arès, R. Temperature Mapping Using Single Wavelength Pyrometry during Epitaxial Growth. *J. Vac. Sci. Technol., B:Nanotechnol. Microelectron.:Mater., Process., Meas., Phenom.* **2011**, *29* (6), 060604.

Downloaded from pubs.acs.org/apchd5/article-pdf/13/17/5139/6652304/acsphotonics.6c01167.pdf by NATL INST FOR MATLS SCIENCE (NIMS) user on 26 October 2026

https://doi.org/10.1021/acsphotonics.6c01167
ACS Photonics 2026, 13, 5139−5146